Forcing of the Martian polar annulus by Hadley cell transport and latent heating

R. K. Scott[1]*, W. J. M. Seviour[2], D. W. Waugh[3]

[1] *School of Mathematics and Statistics, University of St Andrews, St Andrews, UK*

[2] *Cabot Institute, School of Geographical Sciences, University of Bristol, Bristol, UK*

[3] *Department of Earth and Planetary Sciences, The Johns Hopkins University, Baltimore, Maryland, USA*

*Correspondence to: R. K. Scott, School of Mathematics and Statistics, University of St Andrews, North Haugh, St Andrews, KY16 9SS, UK. Email: rks4@st-andrews.ac.uk

---

A hierarchy of idealized models is used to investigate the roles of Hadley cell forcing and latent heat release from carbon dioxide condensation in determining the annular potential vorticity structure of the Martian winter polar vortex. The angular momentum conserving Hadley cell model of Lindzen and Hou with summer hemisphere heating maximum of appropriate strength and latitude produces a strong westerly jet near 60N, similar in strength to the winter polar night jet on Mars. Although the corresponding potential vorticity profile in the angular momentum conserving and thermal wind regions has no annular structure resembling the Martian one, there is an implied delta-function at the discontinuity in zonal wind. This delta-function is smoothed out by explicit diffusion in full axisymmetric model integrations forming a partial annular structure, though a local maximum in potential vorticity at the pole persists and is further enhanced when cooling representing the polar night is included. A distinct a polar minimum and clear annular potential vorticity structure is obtained, however, when an additional representation of polar latent heating is also included. Full eddy-permitting shallow water model integrations confirm the basic structure obtained by the axisymmetric model and suggest a nominal value of viscosity appropriate as a representation of the effects of eddy mixing. Instability of the polar annulus leads to vacillation type behaviour involving eddy growth and annulus disruption, followed by reformation under the influence of radiative relaxation. The degree of transience and mean eddy activity both show an increase with stronger latent heating and a resulting deeper polar potential vorticity minimum, showing that mixing in polar regions may be dependent on details of polar carbon dioxide condensation. Vacillation timescales are also shown to vary with radiative timescale, but through a modification of instability growth rate rather than direct radiative restoration.

Key Words: Mars, polar vortex, Hadley cell, potential vorticity, latent heating
Received ...
Citation: …

1. Introduction

The Martian polar atmosphere in Northern hemisphere winter is characterized by a strong cyclonic zonal mean circulation, the detailed structure of which has been inferred from the temperature retrievals of the Mars Global Surveyor (Banfield *et al.* 2004; McConnochie 2007) as well as model studies (Barnes and Haberle 1996; Waugh *et al.* 2016) and reanalysis products (Montabone *et al.* 2006; Greybush *et al.* 2012; Montabone *et al.* 2014). The polar winds broadly resemble those of the Earth's winter stratospheric polar vortex but with some important differences, in particular regarding the potential vorticity distribution and the forcing mechanisms responsible for creating the circulation (e.g. Mitchell *et al.* 2015, for a comparative overview). Specifically, the Martian polar vortex is observed to have an annular structure in potential vorticity, which has been proposed to be related to latent heat release from condensation of carbon dioxide in the extremely cold temperatures of the polar night (Toigo *et al.* 2017). Since such a structure is expected to be unstable to horizontal wave perturbations, the observations raise the question of how it is sustained on timescales of the seasonal cycle.

In contrast to the Earth, the Martian atmosphere does not have a distinct stratosphere and accordingly the Martian polar vortex may be considered as an essentially tropospheric feature. It is driven in part by the outflow from a broad Hadley cell extending from the southern (summer) hemisphere as far as 60° or 70° N and the associated angular momentum transport within this cell (e.g. Leovy 2001). As such, it may be more correctly likened to the Earth's subtropical jet (Waugh *et al.* 2016). Because the Martian surface has no oceans and a relatively thin atmosphere, the effective solar heating of the atmosphere is more strongly controlled by the planetary obliquity than on Earth. Consequently there is greater hemispheric asymmetry in the location of maximum heating during the seasonal cycle and greater asymmetry between winter and summer Hadley cell branches. Additionally, large zonal mean topography and, to a lesser extent, orbital eccentricity both contribute to higher effective summer heating in the Southern hemisphere and consequently a stronger and broader Northern hemisphere winter Hadley cell branch than its Southern hemisphere winter counterpart (Richardson and Wilson 2002; Zalucha *et al.* 2010). For this reason, the Martian polar vortex is significantly stronger and more defined in the Northern hemisphere winter.

Details of the structure of the Martian polar vortex are tied to the nature of the angular momentum within the Hadley cell. Angular momentum is transported up to the edge of the cell but not significantly beyond it, where the zonal flow is closer to a state of thermal wind balance with the radiative equilibrium temperature. Depending on details of the radiative equilibrium over the pole, the potential vorticity resulting from the Hadley cell could in certain circumstances maximize near the vortex edge, accounting for the observed annular structure, which has a minimum in potential vorticity over the pole and a maximum around 70° N (Mitchell *et al.* 2015; Waugh *et al.* 2016). However, the connection between Hadley cell and polar vortex structure has not been studied in detail. As will be seen further below, details of the potential vorticity distribution over the pole depend on the relative strengths of Hadley cell angular momentum transport and polar diabatic forcing. Diabatic forcing on Mars is not limited to cooling in the winter night, where temperatures are low enough that latent heat release from carbon dioxide condensation may play a significant role in the seasonal mean temperature budget. In particular, a recent modelling study found that when parametrization of carbon dioxide condensation was removed, the polar vortex remained monopolar and did not develop any annular structure (Toigo *et al.* 2017).

It is well known from theory and numerous modelling studies that annular distributions of potential vorticity can in general be shear unstable (Waugh and Dritschel 1991; Dritschel and Polvani 1992). In the context of the Martian vortex, Seviour *et al.* (2017) demonstrated, in a spherical shallow water model that, in the absence of any external forcing, an annular structure broadly representative of the observered potential vorticity rapidly collapses into a monopolar structure. Seviour *et al.* (2017) examined both the linear and nonlinear nature of this barotropic instability. Typical vortex geometries were found to be linearly unstable to zonal wavenumbers in the range 3–6, with maximum growth rates on time scales in the range of 1–3 sols. Consquently, in nonlinear calculations, the annular structure was found to persist when the vortex was sustained by a relaxational forcing to the initial annular structure on comparable time scales, broadly representative of the radiative relaxational time scale on Mars Eckermann *et al.* (2011). Seviour *et al.* (2017) found that when relaxation timescales were much longer than the timescale for instability the late-time vortex became more monopolar, whereas when relaxation timescales were short the late-time vortex remained more strongly annular. When instability and relaxational timescales are comparable, the nonlinear eddy motions that exist in the statistically stationary state represent a balance between zonal forcing and eddy growth due to instability. Observations indicate zonal asymmetries that may indeed represent coherent potential vorticity structures resulting from the instability of a continuously forced annulus.

In this paper, we consider the extent to which the simple Hadley cell models of Held and Hou (1980) and Lindzen and Hou (1988), which have a long history of application in the Earth's atmospheric circulation, may provide insight into how the balance of dynamical forcings controls the structure of the Martian polar vortex. Such axisymmetric models have also been appied to the study of Martian great dust storms (Schneider 1983). In addition to examining the purely axisymmetric formation mechanisms, we also consider how the annular potential vorticity distribution persists in the presence of shear instability and how the saturation of nonlinear eddy motions arising from the instability depends on the relative strengths of Hadley cell transport and diabatic forcing. In the nonaxisymmetric calculations, the paper extends the work of Seviour *et al.* (2017) primarily in that the forcing is a now closer representation of the angular momentum transport on Mars. Specifially, the polar annulus is forced not through a direct relaxation to a prescribed annular structure, but rather through a relaxation to an unrealizable equilibrium state that implies the development of a latitudinally broad Hadley cell.

The paper is structured as follows. In section 2, we review the angular momentum conserving (AMC) models of steady axisymmetric flow and consider the structure of the solutions in the parameter regime relevant for the Martian Northern hemisphere winter solstice. We also introduce simple representations of diabatic cooling and heating within the thermal equilibrium of the polar region. In section 3, we examine the extent to which the AMC model solutions are realized in an axisymmetric shallow water model with relaxation to a similar thermal equilibrium profile and examine how the inviscid solution is approached with decreasing viscosity. We also consider briefly how this model, for a given viscosity appropriate to nonlinear eddy mixing, may be used to quickly infer the zonal mean circulation under different conditions, varying the planetary obliquity and solar forcing. In section 4, we consider the competition between dynamical instability and forcing by examining a full eddy resolving shallow water model. The dependence of the eddy structure of the annulus on different forcing parameters is also considered. Section 5 concludes.

2. The LH88 AMC model

Held and Hou (1980) and Lindzen and Hou (1988) (hereafter LH88) examined the steady state axisymmetric circulation generated by a solar heating that maximized in the tropics. The symmetric case in which the heating maximum is located exactly on the equator (Held and Hou 1980) can be considered as representing equinox conditions, while the off-equator case (LH88) pertains to solsticial or seasonally evolving conditions and is the relevant model for the present study. In these models, the heating is represented by a relaxation to a radiative-convective equilibrium temperature

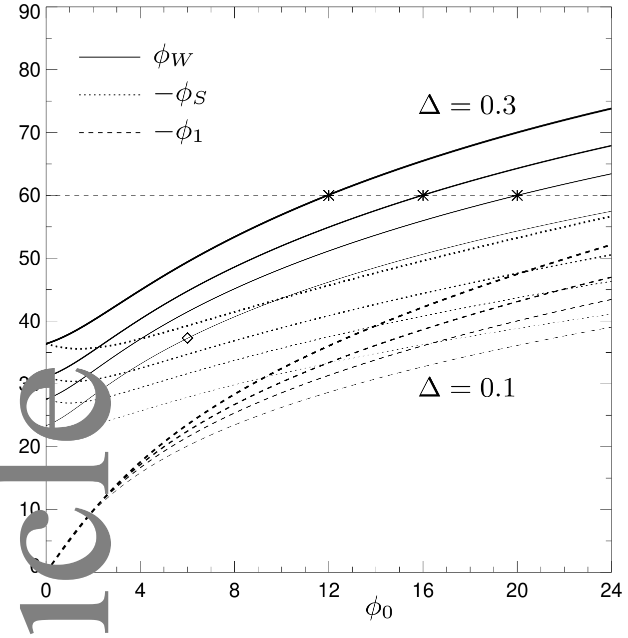

Figure 1. Transition latitudes for the AMC solutions of LH88. The values $\Delta = 0.1, 0.15, 0.2, 0.3$ are shown with increasing line thickness. Stars indicate cases presented below; the diamond indicates that of LH88 Fig.9c.

θ_e. The models are based on the result that the zonal flow in thermal wind balance with such a heating would have a surface wind maximum that exceeds the planetary rotation, which is unrealizable in the absence of additional forcings (Hide 1969). The radiative equilibrium state thus cannot be attained in a latitudinal band surrounding the heating maximum, and the difference between actual temparature θ and θ_e implies the existence of a transverse circulation in the meridional plane. The existence of the transverse circulation in turn means that the absolute angular momentum must be constant within such a region.

The model is made explicit by consideration of the zonal momentum equation, which for steady, axisymmetric flow simplifies to

$$v\frac{dm}{d\mu} = 0, \tag{1}$$

where $m = a\cos\phi(a\Omega\cos\phi + u)$ is the absolute angular momentum, u and v are zonal and meridional components of velocity, ϕ is latitude, $\mu = \sin\phi$, Ω is the planetary rotation, and a is the planetary radius. Equation (1) can be satisfied by the vanishing of either factor. Thus, inside the angular momentum conserving (AMC) region near the heating maximum, $v \neq 0$ but the flow has constant angular momentum, $dm/d\mu = 0$, or equivalently zero absolute vorticity; the associated zonal flow is in thermal balance with a $\theta \neq \theta_e$. Outside the AMC region, $v = 0$ and the zonal wind is in thermal balance with θ_e.

LH88 used a hemispherically asymmetric equilibrium heating with a latitudinal profile of the form

$$\theta_e/\theta_0 = 1 + \Delta((\tfrac{1}{3} - (\sin\phi - \sin\phi_0)^2), \tag{2}$$

where here θ_e represents an average in the vertical over the depth H of the troposphere. The heating has a maximum at latitude ϕ_0 and horizontal temperature difference Δ. In their model formulation, the flow is assumed to be angular momentum conserving between latitudes ϕ_s and ϕ_w, the summer and winter hemisphere termini, and in thermal wind balance poleward of these latitudes. The location of maximum ascent, ϕ_1, differs from the location of the maximum heating, ϕ_0, and is such that the summer cell is significantly weaker than the winter cell. Indeed, one of the main conclusions of LH88 was that even weakly asymmetric forcing results in a large asymmetry between the summer and winter cells, to the extent that the annual averaged transport of seasonally varying heating must greatly exceed the transport due to the annually averaged heating.

For a specified asymmetry ϕ_0 and heating strength Δ, the latitudes ϕ_1, ϕ_s, and ϕ_w are determined uniquely by matching conditions between the AMC and thermal wind regions, obtained from conservation of energy and continuity of temperature at ϕ_s and ϕ_w. The matching conditions were given in equations (8)–(11) of LH88 and lead to a system of three nonlinear equations in the unknowns ϕ_1, ϕ_s, and ϕ_w. For completeness and for ease of future use, we provide the equations in the appendix. The main point, however, is that the solutions are controlled by only two parameters: the asymmetry ϕ_0 and the combination $R = B\Delta$, where $B = gH/a^2\Omega^2$ is a planetary Burger number. Thus the effects of the heating strength Δ and physical planetary parameters affect the solution only in the combination $R = B\Delta$, rendering it unnecessary to consider these parameters in isolation. Here we use planetary parameters as given in Seviour *et al.* (2017), essentially $L_D = \sqrt{gH}/2\Omega = 1800\,\mathrm{km}$ with $a = 3390\,\mathrm{km}$, giving $B = 1.12$.

The AMC model is readily extended beyond the Earth regime to one more relevant to the Martian atmosphere simply by considering larger values of ϕ_0 and/or Δ, which can be increased until the northern edge of the AMC region coincides approximately with the observed extent of the Hadley cell on Mars. Figure 1 shows the latitudes ϕ_1, ϕ_s, and ϕ_w as a function of ϕ_0 and for several values of $\Delta = RB$. The symbol $\phi_0 = 6°$ on the curve with smallest Δ indicates the case considered in LH88 Figure 9c. For the Martian atmosphere, a winter terminus at approximately 60°N is appropriate and is indicated by the dotted line. The response at any point on this line can be obtained with an appropriate combination of ϕ_0 and Δ; three combinations are indicated that will be used for further analysis, $(\phi_0, \Delta) = (12°, 0.3)$, $(16°, 0.2)$, and $(20°, 0.15)$. As would be expected, the more symmetric the forcing (smaller ϕ_0) the larger the Δ required to attain the same maximum latitude of the winter cell.

Profiles of θ/θ_0, vertically averaged zonal wind u, and absolute vorticity ζ_a for three combinations of ϕ_0 and R with $\phi_w = 60°$ (indicated by the symbols on Fig. 1) are shown in Fig. 2. The change in imposed temperature difference Δ can be seen in the profiles of θ and to a lesser extent in those of u and ζ_a. Essentially, the parameters controlling the summer and winter extents and the location of maximum extent all vary more or less similarly with ϕ_0; thus fixing ϕ_w results in similar, but not exactly the same, ϕ_s and ϕ_1 and a broadly similar parabolic (in sine latitude) form for u. The differences will be explored more in the eddy resolving model below.

In all three cases, the absolute vorticity is exactly zero within the AMC region (bounded by the thin vertical lines) and equal to a profile in thermal wind balance with θ_e outside. At first sight, there is no suggestion of a nonmonotonic, annular distribution as found in the Martian reanalysis. In fact, the profiles shown all have a clear polar maximum of absolute vorticity, a consequence of the thermal wind balance with the equilibrium state θ_e. However, the absolute vorticity profiles shown in Fig. 1 hide one fundamental aspect, namely that, regardless of the details of the polar θ_e, the LH88 solution has a discontinuity in the wind profile at ϕ_w, a shear line with an implied δ-function of vorticity. In a viscous model or in a model with resolved eddy mixing, such a shear line would be smoothed out over a finite latitude, with the δ-function broadening but retaining a local maximum. Thus the profiles shown do suggest some form of annular potential vorticity distribution might arise purely as a result of the Hadley cell outflow, but to predict the detailed horizontal structure requires a model in which the transition between AMC and equilibrium regions is correctly represented. This will be addressed in the following two sections.

Before turning to the full dynamical equations, however, we note that the details of the polar vorticity depend only on the θ_e poleward of ϕ_w. Also, provided $\theta_e(\phi_w)$ itself is unchanged, the AMC winds are unaffected by changes to θ_e poleward of ϕ_w, since they are determined purely by matching conditions involving θ at the transition latitudes. Therefore, by modifying θ_e poleward of ϕ_w the polar vorticity profile can be changed directly, without altering the AMC circulation and vorticity structure south of ϕ_w.

To illustrate, we consider how the solution changes when θ_e is modified to $\theta_e + \theta_e'$, where

$$\theta_e'(\phi_c, Q) = Q\theta_0 \cos^2\left(\frac{\pi}{2}\,\frac{\phi - \pi/2}{\phi_c - \pi/2}\right). \tag{3}$$

Here, $Q < 0$ corresponds to an additional cooling and $Q > 0$ to a heating. With $\phi_c = \phi_w$ the modification is restricted poleward of ϕ_w. The response to the cases $Q = \pm 0.1$ are shown dotted and dashed in Fig. 1. Cooling the pole (lowering θ_e) causes the polar maximum in absolute vorticity to increase, as well as the zonal velocity, in accordance with thermal wind balance. Conversely warming causes a decrease in the vorticity over the pole and an increase towards ϕ_w, resulting in a clear nonmonotonic profile and polar minimum, even neglecting the contribution

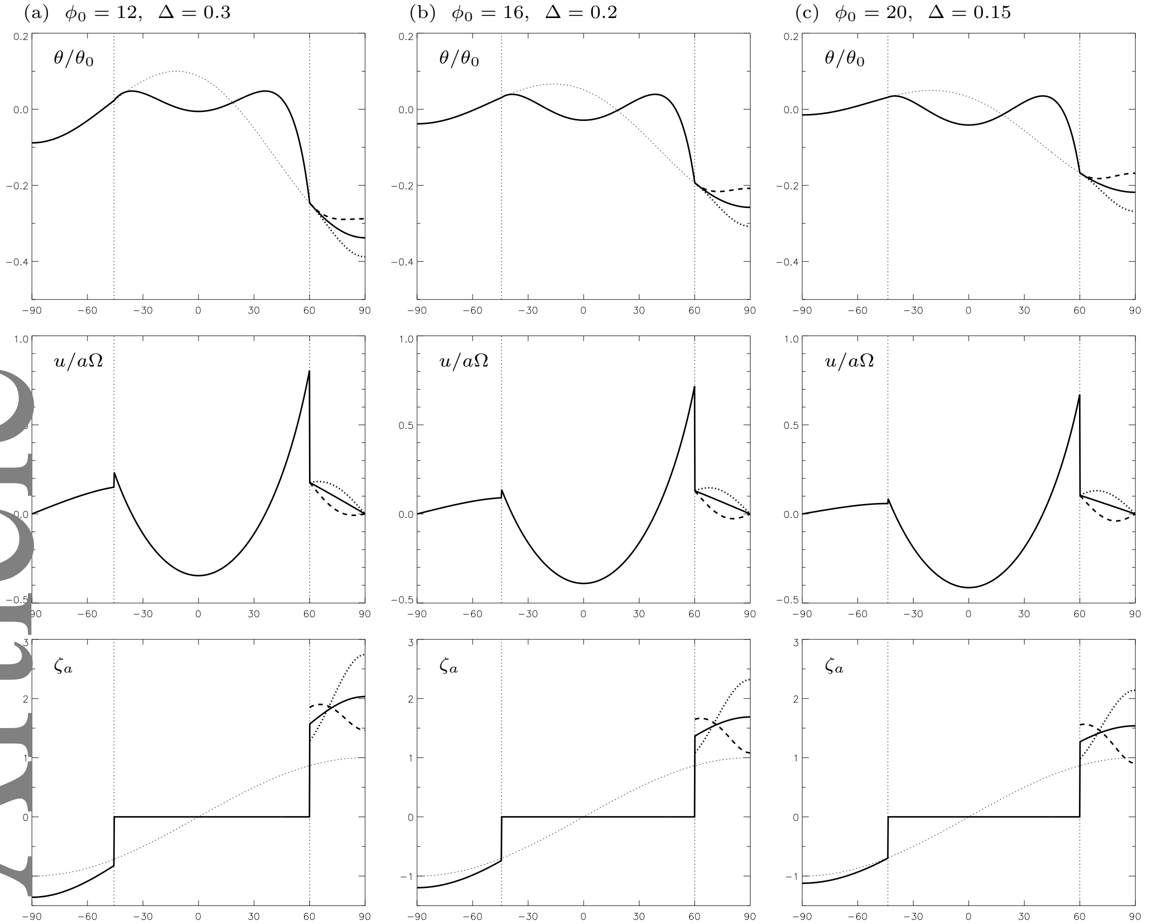

Figure 2. Profiles of θ/θ_0, u, and ζ_a, for solutions of LH88 with $\phi_w = 60°$. Vertical dotted lines indicate ϕ_w and ϕ_s. Thin dotted curve in the top panels indicates θ_e/θ_0. Dotted/dashed curves between 60° and 90° represent with the equilibrium solutions with additional polar cooling/heating.

from the shear line. The case $Q < 0$ may be thought of as a crude representation of radiative cooling in the polar night, and the case $Q > 0$ a representation of latent heat release from carbon dioxide condensation. The two effects and their interaction with the Hadley cell may therefore be considered through the response to a single forcing term in the temperature equation.

3. Full axisymmetric solutions

3.1. Convergence to the AMC solutions

Following LH88, we next compare the AMC solutions with steady solutions obtained following the time-evolution of a full axisymmetric model. Whereas LH88 solve the axisymmetric primitive equations, here we take adantage of the relatively simple vertical structure of the solutions and compare instead with an axisymmetric shallow water model. In this formulation, introduced by Held and Phillips (1990), the meridional component of the shallow water velocity represents the depth average meridional velocity of the Hadley cell. Thermal forcing is represented by a relaxation on the height field to a function h_{eq} which is exactly equivalent to the depth average θ_e/θ_0 of (2), with the mass loss associated with this source term corresponding to a notional vertical velocity out of the layer. Our reasons for comparing with a single-layer representation rather than the full primitive equations are partly numerical efficiency, since in the full eddy resolving calculations of the next section a relatively high resolution is required to capture the eddy dynamics of the annulus instability; and partly because it is desirable to use the simplest model that captures the relevant dynamical processes, here the lateral transport of angular momentum and subsequent instability associated with the horizontal shear. The single-layer representation necessarily neglects details such as the return flow in the boundary layer and allows us to examine the horizontal

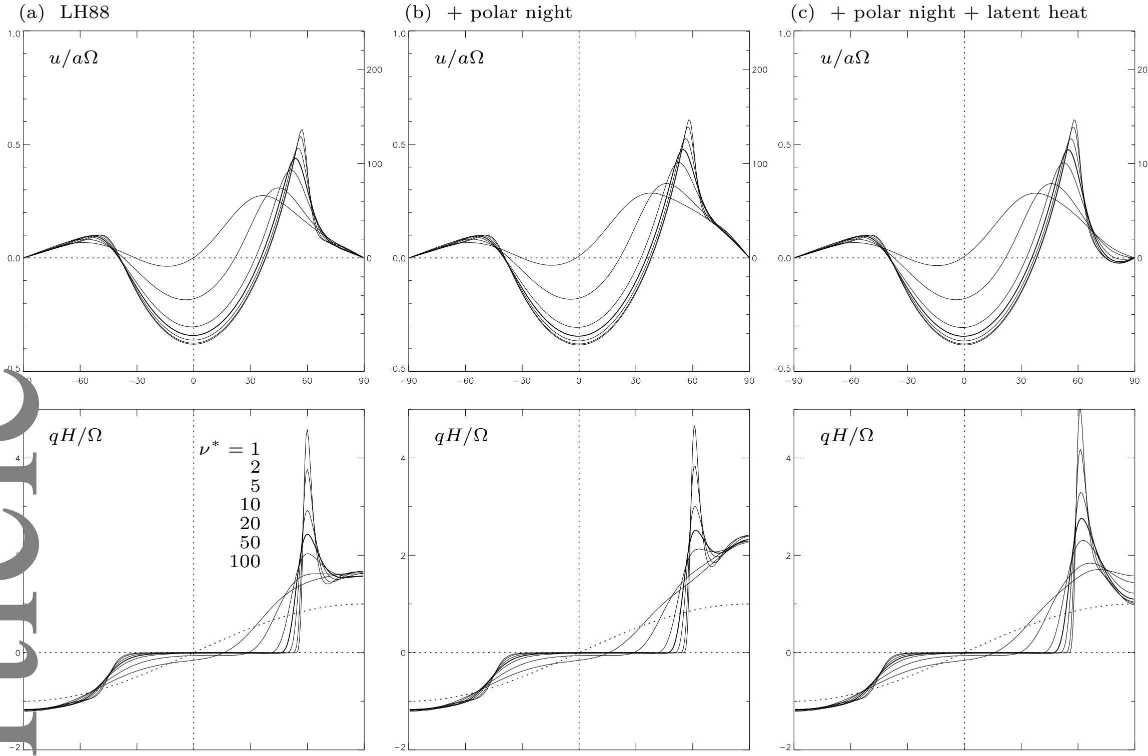

Figure 3. Full (axisymmetric) model solutions with parameters as in Fig. 2(b) and diminishing viscosity, $\nu^* = \nu N(N+1)\Omega/2\pi a^2$, $N = 170$, for different choices of h_{eq}: (a) LH88 profile; (b) LH88 profile with enhanced polar cooling ($\phi_c = 45$, $Q = -0.1$); (c) LH88 profile with enhanced polar cooling ($\phi_c = 45$, $Q = -0.1$) and latent heating ($\phi_c = 60$, $Q = 0.1$). Right-hand ordinate in top panels indicates m/s.

dynamics without the added complications of baroclinic instability.

Figure 3(a) shows the steady state profiles of shallow water zonal velocity u and potential vorticity, $q = \zeta_a/h$ obtained from time integration of the full (axisymmetric) model with relaxation to h_{eq}, where h_{eq}/H is set to the right hand side of (2), and where from now on H is the mean layer depth. The forcing parameters ϕ_0, Δ and Burger number B are the same as used in Fig. 2(b). A viscosity is required in the momentum equations to regularize the delta-function in ζ_a associated with the discontinuity in u of the AMC solution at ϕ_w, with various values of viscous coefficient ν shown. The discontinuity is captured with increasing sharpness with decreasing ν, and the solutions overall appear to be converging steadily to the AMC solution. As in LH88, the location of maximum wind lies a few degrees equatorward of ϕ_w, though appears to be converging to ϕ_w. In the AMC region, the zonal velocity is parabolic (in $\sin\phi$) and the potential vorticity converges to nearly zero. Near the poles both fields attain thermal wind balance with the equilibrium h_{eq}. It is interesting to note that convergence to the AMC solutions appears to be more robust in the shallow water model than in the primitive equations considered by LH88, another factor in favour of their use here. In particular, the potential vorticity did not appear to approach zero in LH88 and the model became transient below a critical viscosity, a phenomenon argued by Schneider (1984) to be due to non-realizability of the AMC solutions.

Convergence to the AMC solutions gives confidence in the accuracy of the AMC model but the limit $\nu \to 0$, with its discontinuity in zonal wind, is not particularly realistic. In a full, eddy resolving model, shear instability would be expected to mix potential vortcity and smooth the discontinuity. Viscosity can therefore be considered as a simple representation of horizontal eddy mixing, at least to the extent that eddies mix potential vorticity downgradient Comparison with the eddy-resolving calculations presented in the next section, suggests that a value $\nu = 10$, indicated in bold, may be an appropriate choice. With this value of ν, potential vorticity has a local maximum near 60°, about

50% in excess of the polar value, while there is an additional weak local maximum at the pole itself. There is a suggestion of an annular structure but no clear minimum over the pole.

3.2. *Effect of polar heating*

While the LH88 h_{eq} (or θ_e) profile provides a simple representation of the seasonal asymmetry in tropical heating, it only partially represents the strong cooling of the winter polar night. The effect of changing the profile in the polar regions to explicitly include the effect of polar cooling are a straightforward consequence of thermal wind balance north of ϕ_w. Here we add an additional cooling of the form (3) with $\phi_c = 45^\circ$ and $Q = -0.1$, similar to, but slightly broader than, the dotted line of Fig. 2(b). The resulting u and q profiles are shown in Fig. 3(b). There is a slight increase in both the zonal velocity and potential vorticity over the pole, including a slight increase in the maximum jet speed, in thermal wind balance with the modified h_{eq}, but very little change to the AMC circulation, even although here the extra cooling does extend partially into the AMC region.

Adding next an additional perturbation to h_{eq}, of the form (3) with $\phi_c = 60^\circ$ and $Q = 0.1$ as a crude represention of the separate effect of latent heating from carbon dioxide condensation, produces the profiles shown in Fig. 3(c). As with LH88 profiles, there is a hollowing out of the core of the vortex, giving a more robust and distributed annular profile with clear polar minimum, and with the degree of non-monotonicity controlled directly by the magnitude of the heating anomaly: strong heating can reduce the polar potential vorticity toward zero or even negative values. Some amount of additional heating, beyond the original LH88 profile, was in all cases necessary to change the local polar maxima in potential vorticity in Fig. 3(a,b) to a local minimum. Again the profiles south of ϕ_w are comparatively unaffected by the additional heating.

An important point to note is that here both the additional polar cooling ($Q = -0.1$) and polar heating ($Q = 0.1$) have the same magnitudes and at the pole cancel exactly. The differences in the thermal wind arise because we have chosen the profile of the cooling to be broader ($\phi_c = 45^\circ$) than that of the heating ($\phi_c = 60^\circ$). The combined perturbation has $dh_{\mathrm{eq}}/d\phi > 0$ near the pole, corresponding to a reduced zonal wind and potential vorticity. We acknowledge that our representation of latent heating is grossly oversimplified, but the more compact distribution of latent heating can be partially motivated by its dependence on extreme temperature values, compared with the broader cooling arising from the smooth latitudinal variation of insolation (Toigo *et al.* 2017).

3.3. *Parameter dependence*

Before proceeding to examine the effect of eddies on the vortex structure, it is interesting to consider briefly what can be deduced from the axisymmetric model in parameter ranges beyond those relevant for Mars. As noted above the LH88 solutions are determined completely by two parameters: the asymmetry ϕ_0 and the combination $R = B\Delta$, where $B = gH/a^2\Omega^2$ is a planetary Burger number. Planetary parameters such as rotation and stratification therefore affect the solution only by modifying the effective heating amplitude R. The dependence of the solution on planetary parameters is essentially the same as that noted recently by Guendelman and Kaspi (2018) in terms of a thermal Rossby number, proportional to R.

As seen in Fig. 3, the axisymmetric solutions depend strongly on viscosity. To be useful, therefore, an estimate must be made of appropriate eddy viscosity values, and as noted above comparison with the eddy-resolving calculations presented in the next section, suggests a value $\nu = 10$. Using this value, the axisymmetric model provides a crude but quick estimate of possible atmospheric regimes that may arise under different planetary parameters. Fixing the heating and varying ϕ_0, for example, produces the profiles shown in Fig. 4a, which gives an indication of the range of Hadley cell and polar vortex strengths that might have existed on Mars during periods when the planetary obliquity was substantially different from its current value.

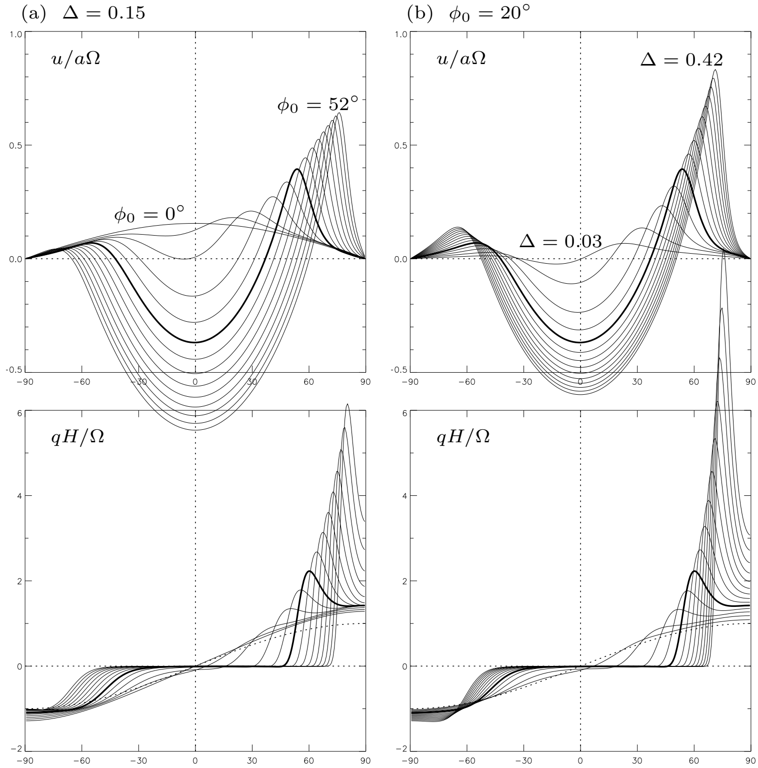

Figure 4. Full (axisymmetric) model solutions with LH88 heating and $\nu = 10$. (a) Fixed $\Delta = 0.15$, ϕ_0 ranging from 0° to 52° in steps of 4°. (b) Fixed $\phi_0 = 20°$, Δ ranging from 0.03 to 0.42 in steps of 0.03.

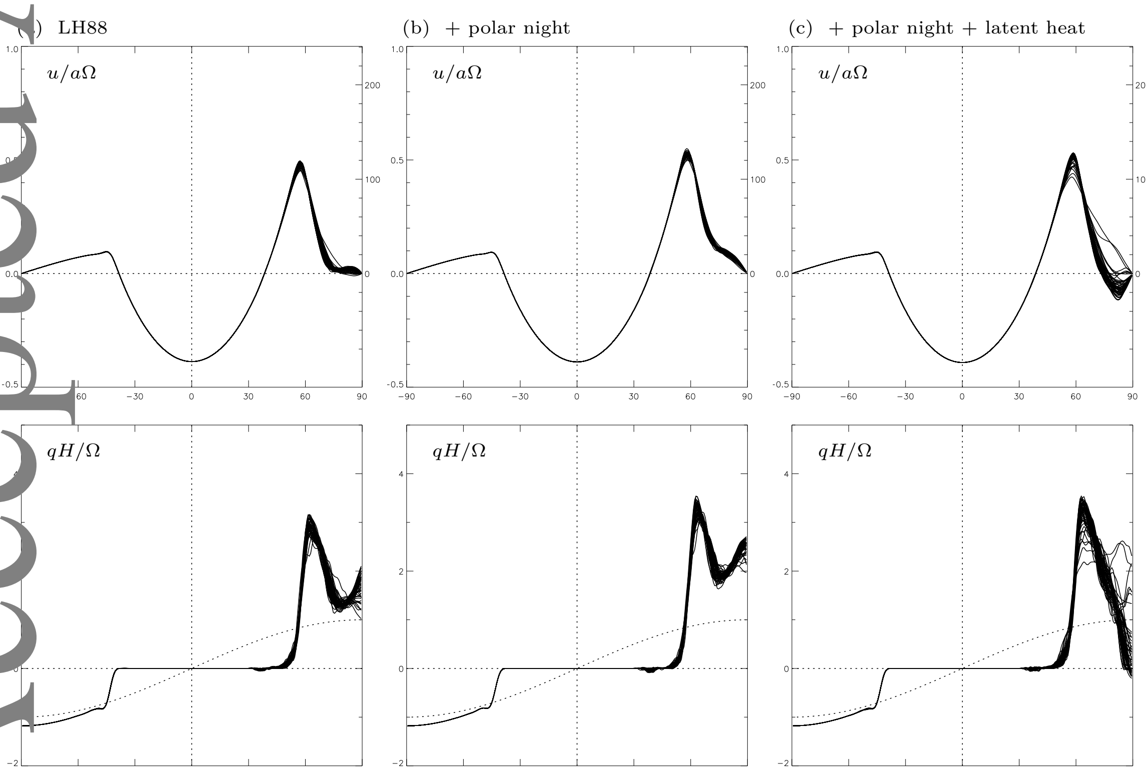

Figure 5. Full eddy resolving model zonal mean fields with parameters as in Fig. 3; lines separated by 10 sol intervals between $t = 1500$ and $t = 2000$. Units for u: $a\Omega$ (left axis), ms^{-1} (right axis). Units for q: 2Ω. Equilibrium h_{eq}: (a) LH88 profile; (b) LH88 profile with enhanced polar cooling ($\phi_c = 45$, $Q = -0.1$); (c) LH88 profile with enhanced polar cooling ($\phi_c = 45$, $Q = -0.1$) and latent heating ($\phi_c = 60$, $Q = 0.1$).

Alternatively, for fixed obliquity, the range of possible circulations that might be obtained with different heating strengths is shown in Fig. 4b. In these calculations, B is fixed at the same (Martian) value used above but the same plot would be obtained by fixing Δ and varying B such that $R = B\Delta$ varies over the corresponding range. This makes explicit how the Hadley cell extent is expected to vary with, say, planetary rotation, all other parameters being equal: lower rotation rate implying larger B, hence larger R and a stronger Hadley cell and more poleward polar vortex. Similarly, at a fixed rotation, stronger stratification would again imply a stronger Hadley cell. As pointed out by Guendelman and Kaspi (2018), of the physical parameters that appear in B, rotation rate is the one that shows the largest variation in relative value, at least among solar system planets.

Of course, come caution is required interpreting such crude estimates; for example, the assumed value of eddy viscosity used here is based on the eddy resolving simulations below and may not be the most appropriate one in other regimes, since eddy length scales will also depend on B (Walker and Scheider 2006). Nonetheless, the above results are consistent with studies in which full general circulation models have been used to estimate the dependence of Hadley cell structure on different planetary parameters. For example, the recent study of Guendelman and Kaspi (2019) found that Hadley cell width increased with increasing obliquity (increasing ϕ_0) and decreasing rotation rate (increasing B), as in Fig. 4.

4. Comparison with an eddy resolving model

4.1. Model details

We next consider the extent to which the axisymmetric annular structure obtained above persists in a full, eddy resolving shallow water model, where the growth of eddies from shear instability is represented. The model equations and physical constants are exactly as described in Seviour *et al.* (2017) (equations 1a-1c, therein) but with no topography, $h_b \equiv 0$, and solved by the same pseudospectral method with triangular truncation at total wavenumber 170 (T170). We consider the "inviscid limit", in the sense viscosity is set to zero, although the model uses a fourth order hyperdiffusion for numerical stability; however, at all but the smallest scales the hyperdiffusion is much less dissipative than the second order viscosity used above. The equilibrium height h_{eq} is as used in section 3, namely the LH88 profile with various combinations of additional polar cooling and heating. The relaxation timescale τ_{rad} is set to 1 sol in most of the experiments, again following Seviour *et al.* (2017) and as suggested by Eckermann *et al.* (2011), with the dependence on this parameter examined in section 4.4 below. A natural extension, not considered here, would be to allow the polar heating to depend interactively on the height field, mimicking the dependence of carbon dioxide condensation on temperature, in a manner similar to that considered recently by Rostami *et al.* (2018).

4.2. Influence of polar heating

Fig. 5 shows the zonal mean zonal velocity and potential vorticity profiles for the same combinations of heating as used in the axisymmetric calculations shown in Fig. 3. Eddies are not explicitly forced in these calculations, but develop from the shear instability associated with the polar potential vorticity distribution. Consequently the flow does not reach a steady state, but does reach a statistical equilibrium on timescales of a few hundred sols. The profiles in Fig. 5 are plotted at 10 sol intervals over the time period $t = 1500$ to $t = 2000$ sols, which gives an idea of the average profile over that period as well as the degree of transience due to the eddy evolution.

Comparing with Fig. 3, it is seen that the zonal mean evolution states of the full shallow water model are quite similar to the axisymmetric solutions with the value $\nu = 10$. In particular, in all cases there is a distinct potential vorticity maximum near 60N and associated jet maximum, resulting from angular momentum transport from lower latitudes in an AMC circulation. Again, the potential vorticity is nearly exactly zero over most of the AMC region. Poleward of 60N, the flow is determined by the details of the additional polar cooling or heating. Only with additional heating over the pole is a distinct polar potential vorticity minimum obtained. In all cases, the relatively small spread of individual lines indicates that the zonal mean

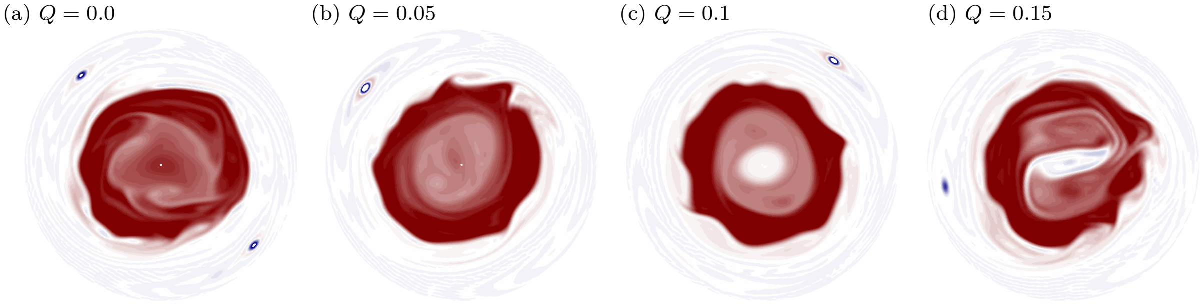

Figure 6. Potential vorticity at $t = 2000$ sols for simulations with latent heaing values $Q = 0, 0.05, 0.1, 0.15$ (a-c). Cases (a) and (c) correspond to the simulations shown in Fig. 5(b,c), respectively.

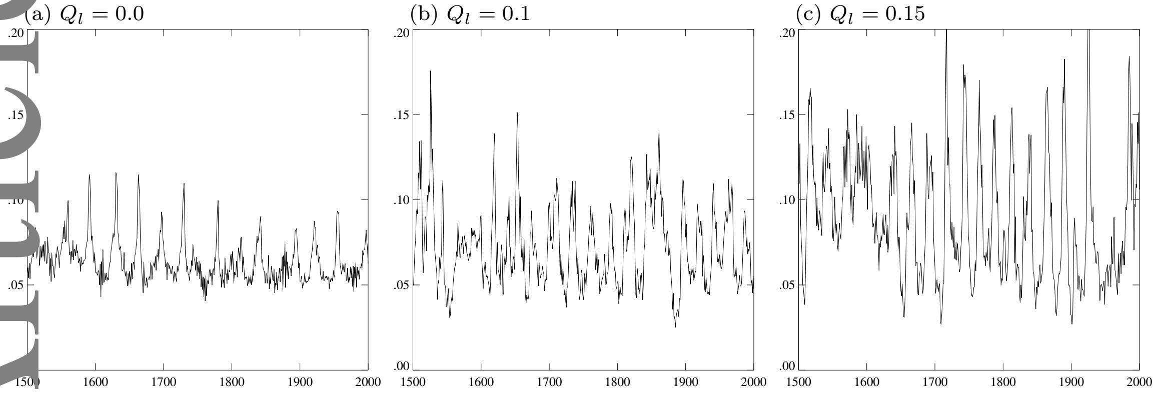

Figure 7. Evolution of eddy enstrophy for cases $Q = 0, 0.1, 0.15$.

flow is persistent in time, despite the instability associated with the non-monotonic potential vorticity. The biggest variations are found in the case with latent heating, where a few individual profiles indicate infrequent but substantial disruptions to the annulus. These are considered in more detail next.

Snapshots of the potential vorticity at $t = 2000$ sols from four integrations with different values of heating $Q = 0, 0.05, 0.1, 0.15$ in (3) (a-d) are shown in Fig. 6, illustrating the effect of increasing latent heating on both the annular structure and the eddy field. The case $Q = 0$ corresponds to Fig. 5a, while the case $Q = 0.1$ corresponds to Fig. 5c. The influence of latent heat is visible in the core, with a deepening potential vorticity minimum for increasing Q.

At first sight, the pattern of eddy activity visible in Fig. 6 is somewhat surprising, with the case $Q = 0.1$ exhibiting the most zonally symmetric annulus of the four, despite having a greater degree of potential vorticity gradient reversal poleward of the jet than the cases $Q = 0.0$ and $Q = 0.05$, corresponding to more unstable vortex. It turns out the anomaly is due to the transient nature of the evolution. This can be illustrated by considering the integrated eddy enstrophy, defined as

$$Z = \frac{1}{4\pi} \int q'^2 dA \qquad (4)$$

where $q' = q - \bar{q}$ is the departure from the zonal mean potential vorticity. The eddy enstrophy, Z, is shown in Figure 7 for the cases $Q = 0.0$, $Q = 0.1$, and $Q = 0.15$ (the case $Q = 0.05$ is similar to $Q = 0.0$) of the time period $t = 1500$ to $t = 2000$ sols. First, there is a small but definite increase in the mean enstrophy with increasing Q (time averaged values of Z are 0.64, 0.69, 0.72, and 0.89, respectively), indicating an overall increase in the eddy activity as the polar potential vorticity minimum deepens, in line with expectations from basic stability considerations. Moreover, there is a substantial increase in the variance of eddy enstrophy, indicating greater transience in the flow at larger Q. In all cases, the time evolution takes the form of quasi-regular vacillations with a characteristic period of

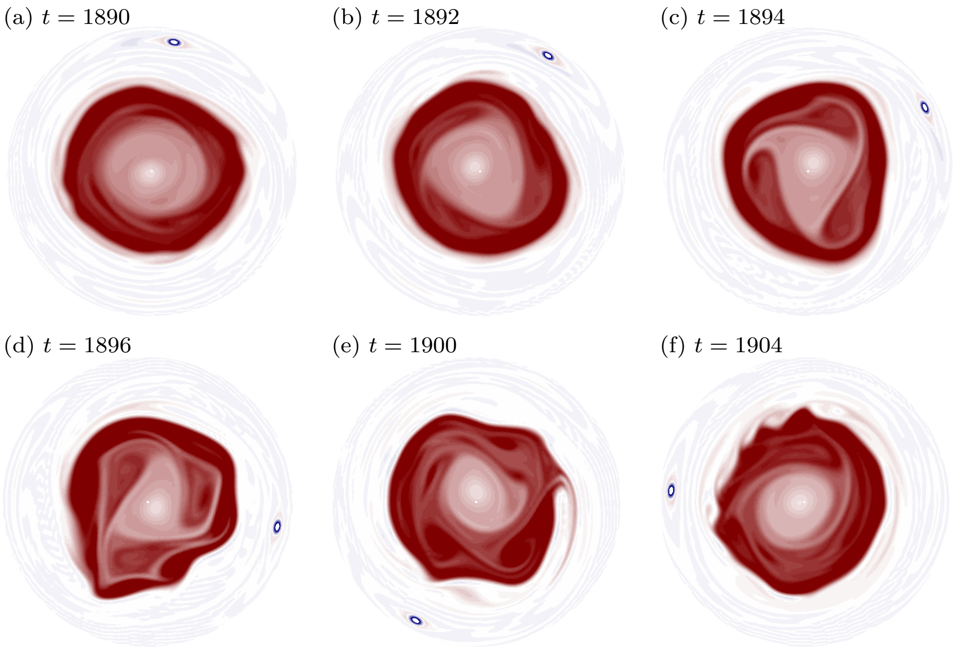

Figure 8. Potential vorticity for case $Q = 0.1$ at times between $t = 1890$ and $t = 1904$ (a-f).

about 20–40 sols that decreases with increasing Q, while the amplitude increases. The strong annularity of the vortex in the case $Q = 0.1$ shown in Fig. 6c is thus associated with the minimum in Z at $t = 2000$ in Fig. 7b. Similarly, the relatively wavy vortex in the case $Q = 0.0$ (Fig. 6a) corresponds to a local maximum in Z at $t = 2000$ (Fig. 7a).

The evolution of the vortex during the course of a typical vacillation cycle is shown in Fig. 8. The plot shows polar potential vorticity at two and four sol intervals between $t = 1890$ and $t = 1904$, while the corresponding eddy enstrophy can be seen in Fig. 7b. At the beginning of this period the polar annulus is well formed and almost completely zonally symmetric, with some weak filamentary structure near the innermost edge remaining from mixing during the previous cycle. Over the next four sols a strong wavenumber three disturbance grows on the inner edge, and subsequently strengthens to the extent that it causes considerable mixing over a region that gradually encroaches deeper into the annulus core ($t = 1900$). Toward the end of the period shown, most of the eddy enstrophy has been dissipated by strong mixing within the annulus and potential vorticity gradients in the interior are reduced overall. The transience found here is reminiscent of, but on shorter timescales than, vacillation cycles identified in simplified models of the Earth's winter stratospheric polar vortex (e.g. Scott 2016), where the vortex is monopolar, shear stable, and the disturbances are forced through planetary wave excitation from the troposphere below. A closer analogy may be found in the rotating annulus experiments of, for example, Young (2014). The cycle shown in Figure. 7 is typical of the annulus evolution between peaks in the eddy enstrophy.

A more extreme example is shown in Fig. 9 for the case $Q = 0.15$ over similarly spaced time intervals between $t = 1922$ and $t = 1936$. Again, a wavenumber three disturbance grows initially on the inner edge, but in this case it grows to large enough amplitudes that the entire annulus is distorted and eventually breaks up completely. Over the next few sols air is mixed vigorously over the entire polar cap, weakening the maximum potential vorticity values. The annular stucture is only gradually recovered from about $t = 1940$ (not shown).

An examination of potential vorticity maps from both the Mars Analysis Correction Data Assimilation (MACDA v1.0) (Montabone *et al.* 2014) and Ensemble Mars Atmosphere Reanalysis System (EMARS) (Greybush *et al.* 2012) reveals a certain amount of variability in the martian

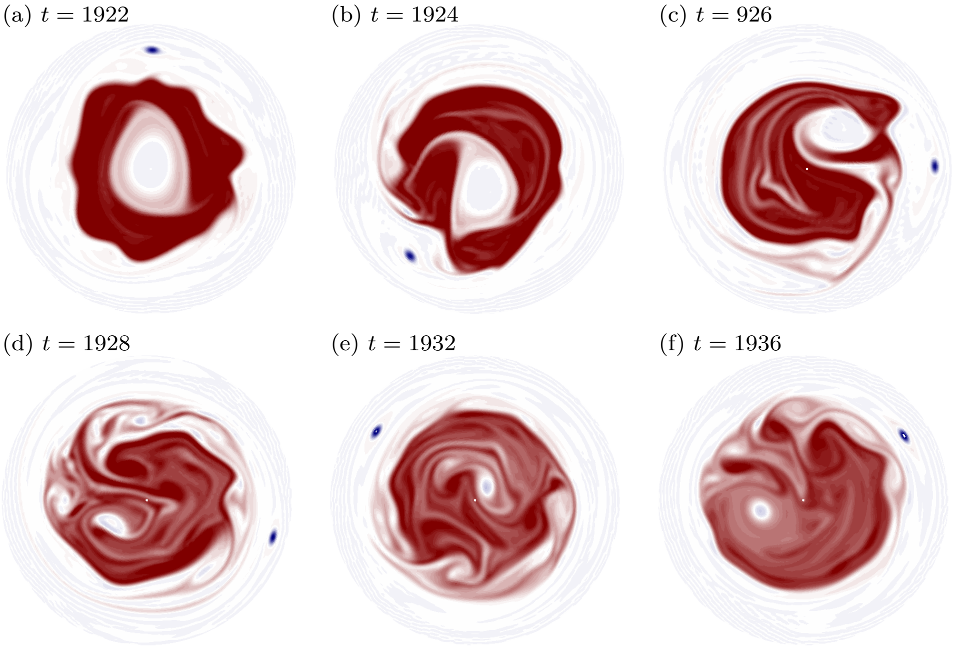

Figure 9. Potential vorticity for case $Q = 0.15$ at times between $t = 1922$ and $t = 1936$ (a-f).

polar annulus not dissimilar to that presented here (see, e.g. Waugh *et al.* (2016), Figure 12 therein). A detailed comparison is complicated in part by the presence of strong topographic variations on Mars, which provides a wave forcing to the annulus that is absent in the model integrations. Transience in the observed wavenumber three can be found, as in Fig. 8, but the evolution likely involves interactions between unstable eddy growth and the fixed topographic forcing. The lower resolution of the reanalysis also makes it harder to follow the Lagrangian evolution of air masses and details of the potential vorticity mixing. As reanalysis improves we anticipate a more careful study of transience will be useful, possibly involving a decomposition into distinct zonal wavenumbers to separate the transience due to unstable growth from that due to topographic interactions.

For completeness, we note that all four cases considered in Fig. 6 exhibit one or two strong compact anticyclones at lower latitudes, around 30N, in the region of near zero potential vorticity in the AMC region. At first these were thought to be numerical artifacts, possibly arising from the overshoots associated with the hyperdiffusion. Further integrations have been carried out at various resolutions and with different forms of small-scale diffusion, including ordinary viscosity. In all cases, similar anticyclones were obtained and appear to be properly resolved dynamical features. They develop at early times in the model evolution at the onset of the first instability of the shear zone at the edge of the AMC region, and appear to arise from the interaction of the wave breaking with the strong relaxation on the height field. Once formed, they persist, largely independently of the flow at high latitudes. Because they are comparitively small-scale features, their influence on the polar dynamics is presumably weak; their scale in relation to the main polar vortex can be inferred from the small dip in zonal mean profiles in Fig. 5. While interesting, and possibly important for the dyanamics at lower latitudes, they lie beyond the scope of the present work and will not be pursued further here.

4.3. *Influence of Hadley cell*

As discussed in section 2, different combinations of heating asymmetry and heating magnitude can combine to produce the same edge ϕ_w of the AMC region. The AMC solutions for the three particular choices $(\phi_0 = 12, \Delta = 0.3)$,$(\phi_0 = 16, \Delta = 0.3)$, $(\phi_0 = 20, \Delta = 0.15)$ were shown in Fig. 2. We ran the full eddy resolving model with the same

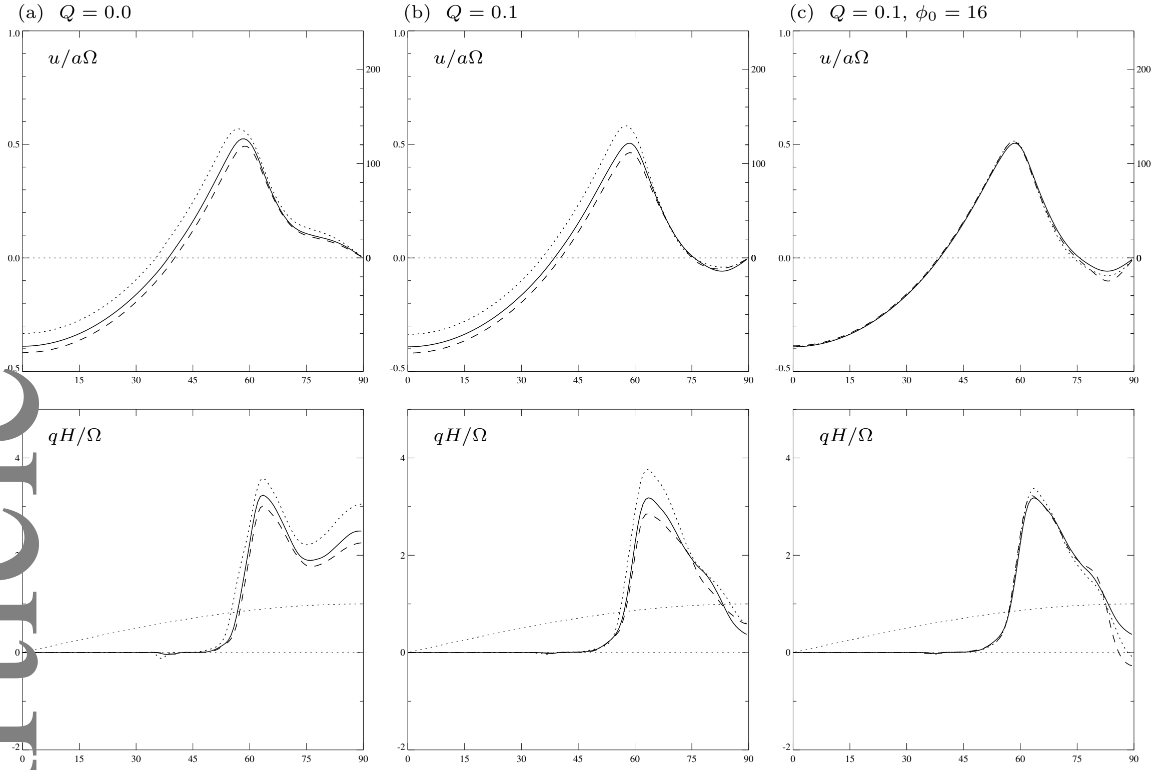

Figure 10. (a,b) Time-averaged (1500-2000 sol) zonal mean zonal velocity and potential vorticity profiles for cases with Hadley cell forcing $\phi_0 = 12$S, $\Delta = 0.3$ (dotted), $\phi_0 = 16$S, $\Delta = 0.2$ (solid) and $\phi_0 = 20$S, $\Delta = 0.15$ (dashed): (a) with no latent heating; (b) with latent heating ($Q = 0.1$). The panel (c) shows the corresponding quantities for the case $\phi_0 = 16$S, $\Delta = 0.2$ with latent heating, and for values of $\tau_{\text{rad}} = 0.5$ (dotted) and $\tau_{\text{rad}} = 2$ (dashed), with the case $\tau_{\text{rad}} = 1$ (solid) shown again for comparison.

parameters, with enhanced polar cooling as above, and with and without additional polar latent heating. The zonal mean zonal velocity and potential vorticity profiles are shown in Figure 10, where the profiles have been averaged in time from $t = 700$ to $t = 1000$ for clarity.

The dependence of the AMC flow on ϕ_0 is similar to the solutions shown in Fig. 2, with slightly higher zonal velocity values across the tropics for $\phi_0 = 12$, decreasing with ϕ_0, regardless of the details of the polar heating. The zonal velocity at the vortex edge shows a similar dependence, as does the peak potential vorticity. The differences are relatively small, compared with the two-fold change in the pole-to-equator equilibrium height difference across this range of Δ.

To measure the extent to which the peak potential vorticity values at ϕ_w influence the stability of the vortex, we again consider the eddy enstrophy, as defined by (4). For the three cases with polar heating shown in Figure. 10b, we show in Figure 11 the integrated eddy enstrophy as a function of time. the case $\phi_0 = 16$ has been repeated for easy reference. Eddy enstrophy is largest for the case $\phi_0 = 12$, consistent with the higher peak potential vorticity of the annulus in that case, and decreses with increasing ϕ_0: time-mean values over the period shown are 0.102, 0.072, and 0.058 respectively. Aside from the decrease in mean values, the variance and characterisic time scales of the variability are broadly similar across the three cases. Clear vacillation cycles occur in all cases, exhibiting somewhat less regularity with increasing ϕ_0, at least over the time interval shown.

4.4. *Influence of radiative timescale*

Finally we consider briefly the effect of τ_{rad} on the eddy evolution of the annulus. On Mars, the radiative timescale is short and tightly controls the thermal wind solution poleward of ϕ_w. However, the Hadley cell itself is established on much longer timescales, typically of the order of 500 sols for the cases discussed above. While we expect the radiative timescale to affect the polar dynamics in a manner similar to that discussed in Seviour *et al.* (2017), such as weaker annular stability at larger τ_{rad}, it

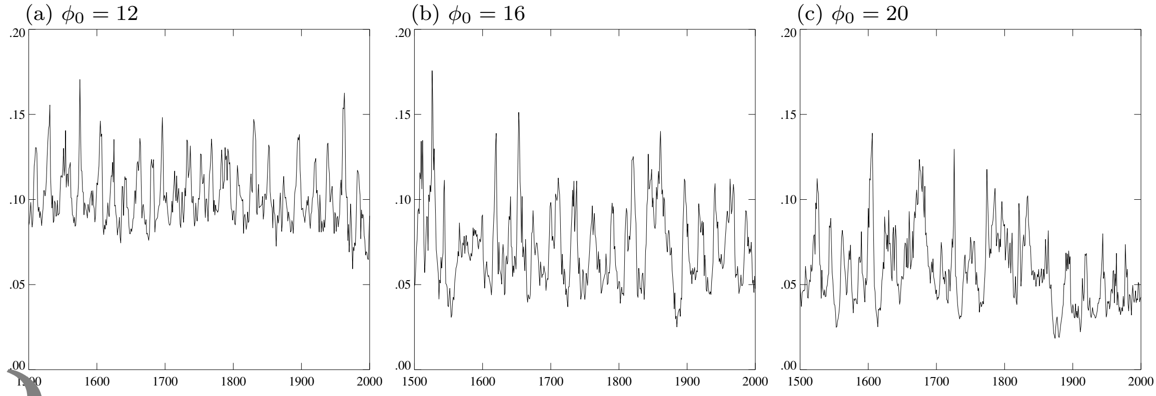

Figure 11. Eddy enstrophy evolution for the three cases shown in Fig. 10b

is possible that differences may arise due to the way in which the Hadley cell forces the potential vorticity structure on longer timescales. We consider, therefore, two further simulations in which the value of $\tau_{\text{rad}} = 1$ sol used in the previous section was increased or decreased by a factor two, keeping all other parameters fixed. *

The zonal mean zonal velocity and potential vorticity profiles for the range of τ_{rad} are shown in Fig 10c. Both cases $\tau_{\text{rad}} = 0.5$ (dotted) and $\tau_{\text{rad}} = 2$ (dashed) are almost identical to the case $\tau_{\text{rad}} = 1$ (solid) previously examined, except very close to the pole, where there are small variations in the minimum potential vorticity attained. Care has been taken to ensure that the averaging period lies well after the flow has reached a statistically stationary state, in all cases.

The eddy enstrophy for these simulations are shown in Fig 12, where again the case $\tau_{\text{rad}} = 1$ has been repeated for easy reference. $t = 1000$ and $t = 1100$. Fluctuations in the eddy enstrophy again take the form of quasi-regular vacillation cycles, with characteristic period decreasing with τ_{rad} from about 50 sols at $\tau_{\text{rad}} = 2$ to about 20 sols at $\tau_{\text{rad}} = 0.5$. In all cases the characteristic period is very short compared with the time scale for equilibration, but very long compared with the radiative timescale.

Perhaps surprisingly, the mean eddy enstrophy increases with decreasing τ_{rad}. It might be expected that the stronger relaxation over the pole would keep the potential vorticity more tightly constrained in an zonally symmetric annular form. However, it should be remembered that the annular structure here is generated indirectly through the Hadley cell forcing, rather than by direct radiative forcing (again, the main difference between the current formulation and that of Seviour *et al.* (2017)). Aside from the increase in the mean, the amplitudes of the cycles (peak to peak change) are not strongly dependent on τ_{rad}.

Other differences in the character of the vacillations can be seen on closer comparison of the $\tau_{\text{rad}} = 2$ and $\tau_{\text{rad}} = 0.5$ cases. The longer period at $\tau_{\text{rad}} = 2$, for example, appears to be associated with a slower increase in eddy enstrophy toward the peak, with a suggestion of a saw-tooth shape in the interval $t = 1600 - 1800$. In these cases the recovery to annular form occurs relatively quickly. Thus it appears the variation in period with τ_{rad} is more than a simple linear response to the relaxation timescale. To illustrate the difference, four snapshots of the polar potential vorticity from each of the cases $\tau_{\text{rad}} = 2$ and $\tau_{\text{rad}} = 0.5$ are shown in Figure 13. For $\tau_{\text{rad}} = 2$ (panels a–d, note that panels are at 12 sol intervals), there is a relatively slow increase in wave amplitude from the minimum near $t = 1712$ and the maximum near $t = 1748$, and a correspondingly gradual increase in the potential vorticity mixing in the annulus. In contrast, for $\tau_{\text{rad}} = 0.5$ (panels e–h, and note that panels are now at 2 sol intervals), the distortion of the annulus occurs much faster with strong mixing taking place just 6 sols after the minimum. The more rapid development of the instability

---

*Because the representation of latent heating in our model is through a modification of θ_e, changing τ_{rad} changes the absolute heating associated with this modification. To keep the absolute latent heating fixed would require θ_e' to vary inversely with τ_{rad}, changing the equilibrium state and resulting in a large dependence of the polar state on the τ_{rad}. Here we are only interested in the effect of τ_{rad}, keeping θ_e fixed.

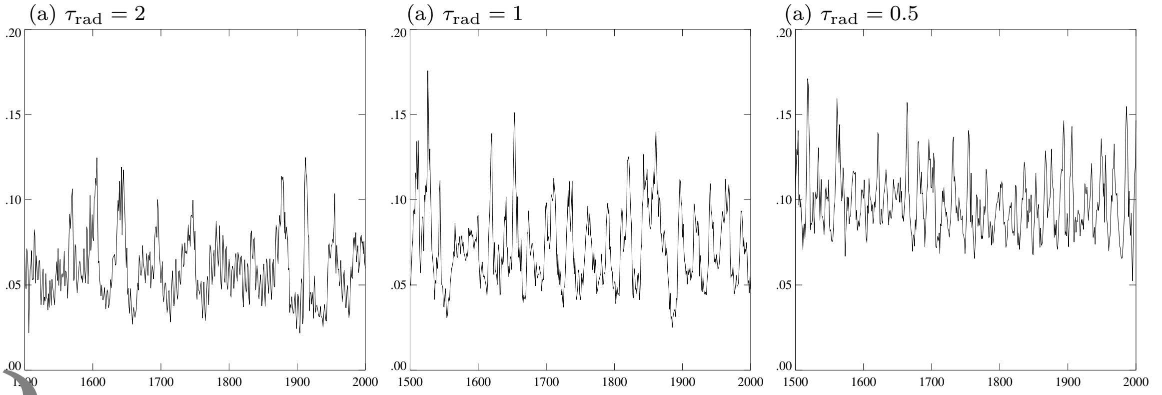

Figure 12. Eddy enstrophy evolution for the three cases shown in Fig. 10c: (a) $\tau_{\text{rad}} = 2$, (b) $\tau_{\text{rad}} = 1$, (c) $\tau_{\text{rad}} = 0.5$; in all cases $\phi_0 = 16$ and $Q = 0.1$.

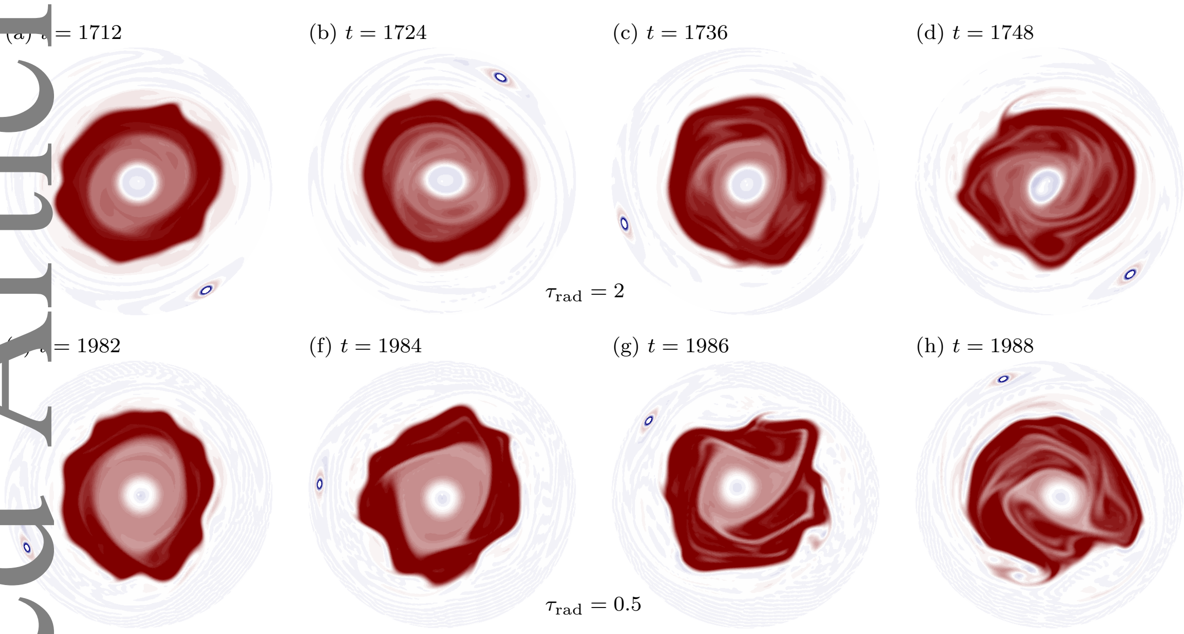

Figure 13. Potential vorticity from simulations with (a–d) $\tau_{\text{rad}} = 2$, corresponding to Figure. 12a, and (e–h) $\tau_{\text{rad}} = 0.5$, corresponding to Figure. 12c, at a set of representative times.

in the latter case cannot be attributed to a direct effect of the shorter radiative timescale, but must arise indirectly through the influence of the zonal mean annular structure on unstable growth rates. It should be noted, however, that such behaviour is by no means universal; all three time series exhibit significant irregularities, and examples of rapid eddy growth also exist at $\tau_{\text{rad}} = 2$ (e.g. $t = 1900$).

5. Conclusions

We have shown that the annular potential vorticity structure of the Martian polar vortex arises naturally from the combination of two basic forcing mechanisms: an angular momentum conserving Hadley cell driven by off-equatorial heating and enhanced heating over the winter pole representing the latent heat release from carbon dioxide condensation. The simplified AMC Hadley cell model of LH88 is capable of capturing the Martian circulation, even though the winter branch of the Hadley cell extends much farther north than on Earth. The model allows the dependence of the polar potential vorticity distribution on each aspect of the forcing to be examined in a clear and unambiguous way. In particular, the location of the zonal wind maximum is controlled mainly by the asymmetry and forcing strength of the Hadley cell, while the details of the flow poleward of the jet are controlled mainly by details of the equilibrium temperature field in that region, through thermal wind balance.

While the potential vorticity structure of the LH88 model shows no explicit annular structure, the infinite shear at the transition latitude implies a delta-function in vorticity that could lead to a local maximum when smoothed by viscosity or eddy mixing in a full model. However, when the latter effects are included, although a potential vorticity maximum is produced near 60°N, there is also a weaker but well defined local maximum over the pole. This local polar maximum is stronger when a representation of the enhanced cooling of polar night is included. To obtain a distinct polar minimum on the other hand, some additional heating is required, the depth of the minimum increasing with increasing heating strength. The result is consistent with the GCM experiment of (Toigo *et al.* 2017) that found a monopolar vortex developed when the parametrization of latent heating from carbon dioxide condensation was turned off, although in our model some degree of the annular structure does arise from the Hadley cell alone. The Hadley cell itself imposes a robust constraint on the location of the maximum of the potential vorticity through the determination of the latitude ϕ_w.

In a full, non-axisymmetric shallow water model with resolved eddies the basic dependence on Hadley cell and additional polar heating was confirmed. In this model, with a radiative relaxation timescale of 1 sol, a stationary state was established on timescales of a few hundred sols, suggesting that the final states are attainable on the timescales of the Martian seasonal cycle. Despite the transience associated with the nonlinear eddy evolution arising from shear instability of the annulus, the basic annular structure persists in the time mean. Typically, eddy amplitudes were found to grow over timescales of a few sols, saturate and then cause transient mixing of the annular structure. When the eddies are strained to small scales and dissipated the annulus is able to reform under the action of the direct radiative forcing to the thermal wind in the polar regions, giving rise to vacillation cycles on timescales of a few tens of sols. The amplitude of these cycles increases as the additional polar heating is increased, to the point that the vacillations can result in the complete mixing of the annulus across the polar region. Although the vacillation timescale increases with radiative timescale, the dependence does not appear to be linked to a direct change in the restoration timescale of the annulus under radiative forcing, but rather linked to changes in the growth rate of the eddy activity.

Aside from elucidating the mechanisms that control the annular structure, as discussed in section 3c, the axisymmetric model provides a quick means of exploring possible circulation patterns that may exist on other planets. In particular, the AMC model formulation depends explicitly on only two parameters, the latitude of the off-equatorial heating maximum and the effective heating strength. The latter is a combination of the actual pole-to-equator equilibrium temperature difference multiplied by a planetary Burger number that measures the relative importance of rotation and stratification. Thus low rotation or high stratification is associated with higher effective heating strength and a wider Hadley cell. While more detailed aspects of the dynamics will depend on individual physical parameters, the above suggests that when conducting parameter sweep experiments of possible circulation regimes in exo-planetary atmospheres, the effects of solar luminosity, planetary mass, rotation etc, be initially considered in combination.

Appendix

The latitudes ϕ_w, ϕ_s, and ϕ_1 in the LH88 model are uniquely determined from the latitude of maximum heating, ϕ_0, by imposing the matching conditions (8)–(11) of LH88. These lead to a system of three equations in the unknowns ϕ_w, ϕ_s, and ϕ_1, which we provide here for ease of reproduciblity. In terms of a sine-latitude coordinate $y = \sin\phi$, and writing

$y_0 = \sin\phi_0$ etc, the matching conditions yield the system

$$\frac{(y_s^2-y_1^2)^2}{1-y_s^2} - \frac{(y_w^2-y_1^2)^2}{1-y_w^2} - 2R[(y_s-y_0)^2-(y_w-y_0)^2] = 0$$

$$\left(\frac{(y_s^2-y_1^2)^2}{1-y_s^2} - 2R(y_s-y_0)^2\right)(y_s-y_1) - I[y_s] + I[y_1] + \frac{2}{3}R[(y_s-y_0)^3-(y_1-y_0)^3] = 0$$

$$\left(\frac{(y_w^2-y_1^2)^2}{1-y_w^2} - 2R(y_w-y_0)^2\right)(y_w-y_1) - I[y_w] + I[y_1] + \frac{2}{3}R[(y_w-y_0)^3-(y_1-y_0)^3] = 0$$

where

$$I[y] = -\frac{1}{3}y^3 - y + 2y_1^2 y + \frac{1}{2}(1-y_1^2)^2 \log\frac{1+y}{1-y}.$$

The system can be solved by a suitable iterative scheme (e.g. Broyden 1965). Notice that the solution y_1, y_s, y_w depends only on the latitude of maximum heating y_0 and the combination of heating strength and planetary Burger number $R = B\Delta$.

References

Banfield D, Conrath B, Gierasch P, John Wilson R, Smith M. 2004. Traveling waves in the martian atmosphere from MGS TES nadir data. *Icarus* **170**: 365–403.

Barnes JR, Haberle RM. 1996. The martian zonal-mean circulation: Angular momentum and potential vorticity structure in GCM simulations. *J. Atmos. Sci.* **53**: 3143–3156.

Broyden CG. 1965. A class of methods for solving nonlinear simultaneous equations. *Mathematics of Computation* **19**: 577–593.

Dritschel DG, Polvani LM. 1992. The roll-up of vorticity strips on the surface of a sphere. *J. Fluid Mech.* **234**: 47–69.

Eckermann SD, Ma J, Zhu X. 2011. Scale-dependent infrared radiative damping rates on Mars and their role in the deposition of gravity-wave momentum flux. *Icarus* **211**: 429–442.

Greybush SJ, Wilson RJ, Hoffman RN, Hoffman MJ, Miyoshi T, Ide K, McConnochie T, Kalnay E. 2012. Ensemble Kalman filter data assimilation of Thermal Emission Spectrometer temperature retrievals into a Mars GCM. *J. Geophys. Res. E* **117**: 11 008.

Guendelman I, Kaspi Y. 2018. An axisymmetric limit for the width of the Hadley cell on planets with large obliquity and long seasonality. *Geophys. Res. Lett.* **45**: 13,213–13,221.

Guendelman I, Kaspi Y. 2019. Atmospheric dynamics on terrestrial planets: the seasonal response to changes in orbital, rotational, and radiative timescales. *Astrophys. J.* **881**: 67.

Held IM, Hou AY. 1980. Nonlinear axially symmetric circulations in a nearly inviscid atmosphere. *J Atmos Sci* **37**: 515–533.

Held IM, Phillips PJ. 1990. A barotropic model of the interaction between the Hadley cell and a Rossby wave. *J. Atmos. Sci.* **47**: 856–869.

Hide R. 1969. Dynamics of the atmospheres of the major planets with an appendix on the viscous boundary layer at the rigid bounding surface of an electrically- conducting rotating fluid in the presence of a magnetic field. *J. Atmos. Sci.* **26**: 841–853.

Leovy C. 2001. Weather and climate on mars. *Nature* **412**: 245–249.

Lindzen RS, Hou AY. 1988. Hadley circulations for zonally averaged heating centered off the equator. *J. Atmos. Sci.* **45**: 2416–2427.

McConnochie TH. 2007. Observations of the martian atmosphere: THEMIS-VIS calibration, mesospheric clouds, and the polar vortex. *Ph.D. thesis* **Cornell University**: https://ecommons.cornell.edu/handle/1813/3517.

Mitchell DM, Montabone L, Thomson S, Read PL. 2015. Polar vortices on Earth and Mars: A comparative study of the climatology and variability from reanalyses. *Q. J. Roy. Meteor. Soc.* **141**: 550–562.

Montabone L, Lewis S, Read P, Hinson D. 2006. Validation of martian meteorological data assimilation for MGS/TES using radio occultation measurements. *Icarus* **185**: 113–132.

Montabone L, Marsh K, Lewis SR, Read PL, Smith MD, Holmes J, Spiga A, Lowe D, Pamment A. 2014. The Mars Analysis Correction Data Assimilation (MACDA) dataset v1.0. *Geosci. Data J.* **1**: 129–139.

Richardson MI, Wilson RJ. 2002. A topographically forced asymmetry in the Martian circulation and climate. *Nature* **416**: 298–301.

Rostami M, Zeitlin V, Montabone L. 2018. On the role of spatially inhomogeneous diabatic effects upon the evolution of Mars' annular polar vortex. *Icarus* **314**: 376–388.

Schneider EK. 1983. Martian great dust storms: Interpretive axially symmetric models. *Icarus* **55**: 302–331.

Schneider EK. 1984. Response of the annual and zonal mean winds and temperatures to variations in the heat and momentum sources. *J. Atmos. Sci.* **41**: 1093–1115.

Scott RK. 2016. A new class of vacillations of the stratospheric polar vortex. *Q. J. Roy. Meteor. Soc.* **142**: 1948–1957.

Seviour WJM, Waugh DW, Scott RK. 2017. The stability of Mars' annular polar vortex. *J. Atmos. Sci.* **75**: 1533–1547.

Toigo AD, Waugh DW, Guzewich SD. 2017. What causes Mars' annular polar vortices? *Geophys. Res. Lett.* **44**: 71–78.

Walker CC, Scheider TS. 2006. Eddy influences on Hadley circulations: simulations with an idealized GCM. *J. Atmos. Sci* **63**: 3333–3350.

Waugh DW, Dritschel DG. 1991. The stability of filamentary vorticity in two-dimensional geophysical vortex-dynamics models. *J. Fluid Mech.* **231**: 575–598.

Waugh DW, Toigo AD, Guzewich SD, Greybush SJ, Wilson RJ, Montabone L. 2016. Martian polar vortices: Comparison of reanalyses. *J. Geophys. Res. E* **121**: 1770–1785.

Young RMB. 2014. The Lorenz energy cycle in simulated rotating annulus flows. *Phys. Fluids* **26**: 056 602.

Zalucha AM, Plumb RA, Wilson RJ. 2010. An analysis of the effect of topography on the Martian Hadley cells. *J. Atmos. Sci.* **67**: 673–693.